Acta Pharmaceutica Sinica B 2026;16(5):3175−3190

Chinese Pharmaceutical Association
Institute of Materia Medica, Chinese Academy of Medical Sciences

Acta Pharmaceutica Sinica B

www.elsevier.com/locate/apsb
www.sciencedirect.com

ORIGINAL ARTICLE

Inhalational therapy of pulmonary infection *via* macrophage-targeted nanoemulsions

Hairui Wang[a,b], Jinghong Xian[a,b], Guonian Zhu[a,b], Zhiqiang Xie[c], Guangsheng Du[c], Yongshun Zhang[c], Lan Yang[c], Yunming Zhang[c], Teng Li[c], Yehui Zhou[c], Weimin Li[a,b,*], Xun Sun[c,*], Chengdi Wang[a,b,*]

[a]*Department of Pulmonary and Critical Care Medicine, Institute of Respiratory Health, State Key Laboratory of Respiratory Health and Multimorbidity, West China Hospital, West China School of Medicine, Sichuan University, Chengdu 610041, China*
[b]*Targeted Tracer Research and Development Laboratory, Frontiers Science Center for Disease-related Molecular Network, West China Hospital, West China School of Medicine, Sichuan University, Chengdu 610041, China*
[c]*Key Laboratory of Drug-Targeting and Drug Delivery System of the Education Ministry, Sichuan Engineering Laboratory for Plant-Sourced Drug and Sichuan Research West China School of Pharmacy, Sichuan University, Chengdu 610064, China*

Received 4 September 2025; received in revised form 13 October 2025; accepted 27 November 2025

KEY WORDS

Nanoemulsions;
Inhaled therapy;
Mycobacterium tuberculosis;
Rifampicin;
LCL161;
Macrophages;
Antibiotic;
Immunotherapy

Abstract The dynamic immune landscape within the tuberculous (TB) granuloma microenvironment critically governs antibiotic penetration efficiency, bacterial persistence, and long-term therapeutic outcomes. Herein, we present a macrophage-targeted inhalable nanoemulsion for co-delivering rifampicin and LCL161, an inhibitor of apoptosis protein antagonist. Inhaled mannose-nanoemulsions (named RL-NE@Man) enable granuloma-targeted delivery in TB mice model, increasing infected macrophage apoptosis, remodeling the tuberculosis microenvironment, and promoting T-cell immunity to synergize with antibiotics for the eradication of granulomas and persistent *Mycobacterium tuberculosis infection*. Following two-dose inhalational administration, RL-NE@Man displayed potent bactericidal activity against *M. tuberculosis* while concurrently alleviating pulmonary pathological lesions and hyperinflammatory responses, demonstrating superior bacterial suppression efficacy compared with that of the first-line rifampicin monotherapy. This inhaled combination therapy, which integrates immunomodulators with antibiotics to modulate the local immune landscape and synergistically enhance bactericidal efficacy, represents a novel therapeutic strategy for precision tuberculosis management.

*Corresponding authors.
E-mail addresses: weimi003@scu.edu.cn (Weimin Li), sunxun@scu.edu.cn (Xun Sun), chengdi_wang@scu.edu.cn (Chengdi Wang).
Peer review under the responsibility of Chinese Pharmaceutical Association and Institute of Materia Medica, Chinese Academy of Medical Sciences.

https://doi.org/10.1016/j.apsb.2026.02.026

1. Introduction

Tuberculosis (TB), caused by *Mycobacterium tuberculosis*, remains a major global threat to public health[1]. According to the WHO 2024 Global Tuberculosis Report, in 2023, an estimated 10.8 million people suffer from tuberculosis, with 8.2 million newly diagnosed and reported cases, the highest number since records began[2]. In low- and middle-income countries, TB is a leading infectious cause of death and significantly increases the risk of developing chronic obstructive pulmonary disease[3]. Standard tuberculosis treatment relies on conventional chemotherapy (*e.g.*, rifampicin)[4], but its efficacy is constrained by imprecise targeting of granulomatous lesions and intracellular pathogens[5,6], compounded by the stratified architecture of granulomas that impedes antibiotic penetration into pathological niches[7]. These pharmacokinetic limitations result in subinhibitory concentrations at infection sites, promoting bacterial persistence and resistance evolution through prolonged low-level drug exposure[8,9], which often yields unsatisfactory clinical outcomes[10,11]. Furthermore, this pathogen employs sophisticated immune evasion strategies to circumvent surveillance by other immune effectors, including antigenic masking and interference with phagolysosomal maturation[12,13].

Macrophages constitute the primary host cellular niche for *M. tuberculosis* proliferation while simultaneously functioning as pivotal effector cells in infection control, making them pivotal therapeutic targets for TB intervention strategies[14]. After *M. tuberculosis* infection, macrophages exhibit biased plasticity characterized by a shift from classical M1 macrophages with strong bactericidal activity to M2 macrophages with reduced antimicrobial capacity[15,16]. These M2 macrophages permit the growth of *M. tuberculosis*. The capacity to strategically remodel macrophage responses through immunomodulatory or chemotherapeutic interventions holds promise for optimizing therapeutic outcomes in TB by promoting pathogen clearance and mitigating immunopathology[17]. *M. tuberculosis*-infected macrophage apoptosis facilitates antigen-specific T cell responses, while immunomodulators synergize with antibiotics to enhance bacterial clearance and increase clinical cure rates through combined antimicrobial-immunotherapeutic actions[18]. Moreover, a previous study has demonstrated that promoting apoptosis by using antagonists of inhibitor of apoptosis proteins significantly promotes *M. tuberculosis* clearance[19]. LCL161, a clinical-stage investigational agent primarily evaluated in clinical cancer trials, has demonstrated limited efficacy as a monotherapy, and combination regimens have been employed to improve therapeutic outcomes. Recent preclinical investigations have revealed its potential utility in tuberculosis treatment through mechanisms involving host-directed immune modulation[19]. However, few studies have explored its combined use with established anti-TB agents, leaving a critical gap in understanding its synergistic potential in pulmonary tuberculosis management. Therefore, developing a therapeutic strategy capable of regulating the tuberculosis microenvironment and enabling efficient antibiotic delivery is important for the precise treatment of pulmonary tuberculosis.

Nanoparticle drug delivery presents a promising approach to address these challenges, offering the advantages of co-encapsulation of combination therapies, sustained release, targeted delivery, reduced dosing frequency, and minimized side effects, which may ultimately improve tuberculosis treatment outcomes and patient compliance[20,21]. Studies have demonstrated that nanoparticles can effectively target granulomas (the hallmark lesions of tuberculosis) and achieve prolonged retention through the enhanced permeability and retention (EPR) effect, thereby enabling precise drug delivery[22,23]. A new study revealed groundbreaking progress in nanotherapeutic TB treatment *via* the integration of both active and passive targeting approaches demonstrated[23]. However, these nanoparticles face challenges, including complex manufacturing processes and unavoidable systemic distribution.

Inhalation delivery maximizes drug concentrations in lung tissues while avoiding systemic toxicity and improving patient compliance, making it the preferred route of drug administration for the treatment of respiratory diseases since ancient times[24,25]. Engineered nanomedicine inhalants exploit the biophysical advantages of pulmonary administration to overcome biological barriers in respiratory therapeutics. Therefore, we hypothesized that M2-type macrophage-targeted ligand-modified inhalable nano-delivery systems could maximize access to the site of infection following inhalation administration. Mannose, a naturally occurring monosaccharide with excellent biocompatibility, can bind to mannose receptors on macrophages. Its proven safety profile and good stability make it the most widely used macrophage-targeting ligand[26,27]. Consequently, we propose that the delivery of macrophage-targeting nanomedicine *via* nebulization to tuberculous granulomas will simultaneously (i) induce macrophage apoptosis to disrupt the favorable mycobacterial niche and (ii) remodel the local immune landscape to synergistically promote the antibiotic-mediated clearance of *M. tuberculosis*.

Herein, we engineered a mannose-modified nanoemulsion for the co-delivery of rifampicin and LCL161 (named RL-NE@Man). Nanoemulsions, which are nanoscale emulsions with particle sizes between tens and hundreds of nanometers, have been widely used in recent decades because of their unique structural and performance advantages such as small particle size, biocompatibility, easy loading of active pharmaceuticals, and ease of larger-scale production[28]. The primary excipient DPPC (dipalmitoylphosphatidylcholine), a natural lung surfactant incorporated in nanoemulsions, has received US Food and Drug Administration (FDA) approval for inhalation and offers key benefits including established safety, enhanced macrophage uptake in alveoli, and strong clinical translation potential[29,30]. *In vitro* studies demonstrated that RL-NE@Man was taken up by M2 macrophages and induced apoptosis in these cells. Lower concentrations of RL-NE@Man reduced the number of bone marrow-derived macrophages (BMDMs) differentiated to M2-type macrophages, but unaffected the proliferation of M1-type macrophages. In addition, RL-NE@Man penetrates into the necrotic regions of granulomas and targets intracellular *M. tuberculosis via* specific ligand−receptor

binding in murine tuberculosis models. TB mice in the RL-NE@Man treatment group exhibited a significant reduction in the number of tuberculous granulomas and a significant reduction in the percentage of M2-type macrophages in bronchoalveolar lavage fluid (BALF) and mediastinal lymph nodes and elicited a $CD4^+$ and $CD8^+$ T cell response. Quantitative real-time PCR (qPCR) and immunohistochemical analyses demonstrated that RL-NE@Man effectively decreased the *M. tuberculosis* burden in lung tissues while mitigating pathological lesions and reducing inflammatory responses. This study highlights the critical value of the local microenvironment of tuberculosis in fueling antibiotic sterilization and provides a promising translational therapeutic paradigm for inhaled chemoimmunotherapy for tuberculosis.

2. Materials and methods

2.1. Materials and ethics statement

LCL161 was purchased from BioChemPartner (Shanghai, China). Rifampicin was purchased from MeilunBio® (China). DSPE-PEG_{2000} and DSPE-PEG_{2000}-Mannose were purchased from Ruixi Biotechnology Co., Ltd. (Xi'an, China). A cell counting kit-8 was obtained from Beyotime Biotechnology. An anti-mannose receptor antibody was purchased from Abcam (ab300621). Monoclonal antibodies conjugated with fluorescent tags were purchased from eBioscience or Invitrogen (USA). Specific pathogen-free (SPF) female C57BL/6 mice (6−8 weeks old) were purchased from Beijing HFK Bioscience Co., Ltd. All experimental procedures were conducted in accordance with the recommendations in the Guide for the Care and Use of Laboratory Animals of Sichuan University Ethics Committee. The animal procedures were approved by the Committee on the Ethics of Animal Experiments of Sichuan University (Approval No. SYXK (Chuan) 2023-0113). The animals were maintained in an SPF facility at West China School of Pharmacy with controlled environmental parameters and free access to a regular chow diet and water under a 12-h light/dark cycle. The bacterial infection experiments were conducted in a biosafety level 2 (BSL-2) laboratory certified by the Sichuan Provincial Health Commission, ensuring compliance with national biosafety regulations.

2.2. Cells and M. tuberculosis strains

Human bronchial epithelioid cells (BEAS2B, ATCC) and RAW264.7 cells were maintained in Dulbecco's modified Eagle's medium (DMEM; Gibco, USA). BMDMs were isolated from C57BL/6 mice and cultured in DMEM (Gibco, USA). All media were supplemented with 10% fetal bovine serum (FBS; ExCell Bio, China). Middlebrook 7H10 agar medium and Middlebrook 7H9 medium were purchased from Becton Dickinson and Company (BD, USA). *M. tuberculosis* H37Ra (ATCC25177), mCherry-H37Ra and Middlebrook OADC enrichment were purchased from Gene-Optimal Science and Technology (Shanghai, China).

2.3. Preparation and characterization of RL-NE@Man

On the basis of preliminary screening of the solubility of LCL161 and rifampicin in different oil phases, soybean oil and DPPC were selected as the primary oil phase materials. A ternary component system was established using the BoxBehnken design-response surface method, with concentrations ranging from 0 to 20 mg of soybean oil, 0−40 mg of DPPC, and 0−6 mg of cholesterol. Through the design and execution of 17 experimental designs, the formulation was optimized. Supporting Information Table S1 displays the independent factors of the formulation design and their subsequent outcomes (calculated as given by Design-Expert version 12.0). In brief, rifampicin and LCL161 were dissolved in this mixture with 1.5 mL of chloroform to form the oil phase. The oil phase was then mixed with an aqueous solution containing 0.05% (*w*/*v*) Tween 80 and 0.15% (*w*/*v*) sodium citrate. The mixture was homogenized by vortexing and then sonicated at 200 W for 8 min in an ice-water bath to obtain the RL-NE. To prepare mannose-modified nanoemulsions, DSPE-PEG_{2000}-mannose was incorporated into the RL-NE emulsion system. The mixture was then processed using a high-pressure homogenizer (AH-Nano, ATS, Canada) under the following conditions: homogenization pressure of 800 bar, temperature of 4 °C, and duration of 10 min. For particle size analysis, the nanoemulsion was 10 × diluted with deionized water and characterized by dynamic light scattering (Malvern Zetasizer Nano ZS). The structure of the RL-NE@Man was characterized using a transmission electron microscope (H-600, Hitachi, Japan), and these samples were placed in contact with copper grids with negative staining. The rifampicin- and LCL161-loaded nanoemulsions were separated from the free drugs using Sephadex G-50 (GE Healthcare, USA). A mixed solvent of 1% Triton/acetonitrile/ethanol (1:5:5, *v*/*v*/*v*) was used to completely extract both drugs by ultrasonication for 10 min. The concentrations of rifampicin and LCL161 were determined by high-performance liquid chromatography (HPLC) using a C18 column (Agilent TC-C18(2)) at 30 °C, with the detection wavelength set at 254 nm.

2.4. In vivo distribution

The mice were anesthetized by intraperitoneal injection of tribromoethanol. A nanoemulsion labeled with the fluorescent dye DiD was administered to mice *via* a small-animal microsprayer aerosolizer (BJ-PW-R; BioJane, China). Fluorescence signals were monitored at different time points using a small-animal *in vivo* imaging system (IVIS, Lumina Series, USA).

2.5. Immunofluorescence assay

Lung tissues from mice were embedded in OCT (SAKURA Tissue-Tek®, USA) compound at temperatures below -20 °C. Lung tissues were sectioned at a thickness of 10 μm using a cryostat (Leica, CM1950, Germany), followed by phosphate buffer solution washing, antibody blocking, and anti-CD206 primary antibody (Abcam, USA) staining according to the manufacturer's recommended concentration and incubation time. After 12 h of primary antibody incubation, the tissue sections were incubated with an Alexa Fluor 647-conjugated goat anti-rabbit IgG (H + L) secondary antibody (Abcam, Ab150079, USA) at room temperature for 2 h. Finally, the nuclei were counterstained with DAPI, and immunofluorescence images were captured using a confocal fluorescence microscope (Zeiss, LSM880). The colocalization coefficients and fluorescence intensity were analyzed using a Zeiss confocal microscope software system.

2.6. Antibacterial activity evaluation of RL-NE@Man

Fifty microliters of H37Ra bacilli ($\sim 10^7$ CFU/mL) were mixed with 50 μL of drug-containing medium from different groups in

96-well black plates. The concentration of rifampicin in the different groups ranged from 0 to 20 μg/mL. The 96-well black plates were incubated statically at 37 °C in a bacterial incubator for 10 days. Afterward, 100 μL of sterile resazurin solution (40 μg/mL) was added to each well, followed by an additional 4 h of incubation. The fluorescence/absorbance was measured using a microplate reader. Concentration−response curves were fitted, and EC_{50} values were calculated using GraphPad Prism 10. Following treatment with RL-NE@Man, *M. tuberculosis* H37Ra cells were washed three times with PBS (3000 × *g*, 15 min) and fixed overnight in 2.5% glutaraldehyde prior to morphological analysis by scanning electron microscopy (SEM). For the plate count assay, the initial *M. tuberculosis* suspension (1.0 McFarland standard) was serially diluted to various concentrations. A 100 μL aliquot of each dilution was then plated onto drug-containing Middlebrook 7H10 agar plates and spread evenly using a sterile spreader. Control groups were established in parallel. Bacterial colony growth was observed and recorded on a weekly basis. To quantify the bacterial load in the lung tissues of the mice, homogenates were first prepared by cryogenic grinding. Total nucleic acids were then extracted from the homogenates. Quantitative PCR (qPCR) was performed to target the *Ag85b* gene of *M. tuberculosis* H37Ra for quantification, with B2M and 18S rRNA used as reference genes.

2.7. In vivo therapeutic effect of RL-NE@Man

Female C57BL/6 mice (6−8 weeks old) were randomly divided into five groups of four mice each: PBS, RFP, RFP + LCL161, RL-NE, and RL-NE@Man. The mice were housed under SPF conditions in the Laboratory Animal Facility of West China School of Pharmacy, Sichuan University, with a 12-h light/dark cycle and free access to a standard diet and water. All animal experiments were approved by the Animal Ethics Committee of Sichuan University and conducted in accordance with the Guidelines for the Care and Use of Laboratory Animals established by the Institutional Animal Care and Use Committee (IACUC) of Sichuan University. *In vitro* and *in vivo* experiments associated with *Mycobacterium* were conducted in a biosafety level II laboratory. Under the guidance of preliminary experiments and reference literature, a tuberculosis mouse model was established by aerosol inhalation of H37Ra (10^7 CFU/mL, 40 μL) on Day 0. On Day 22, the mice were administered 30 μL of PBS, RFP, RFP + LCL161, RL-NE, or RL-NE@Man (RFP: 4.5 mg/kg; LCL161: 1.5 mg/kg) *via* inhalation. On Day 25, the same dose as that used for the previous treatment was readministered. On Day 11 posttreatment, the mice were humanely euthanized for lung collection. Bacterial nucleic acid quantification and histological analyses (H&E staining, Ziehl-Neelsen acid-fast staining, and TNF-α, IL-6 and IL-1β immunohistochemistry) were performed on lung tissues. Concurrently, the levels of proinflammatory cytokines (IL-6, TNF-α, and IFN-γ) in bronchoalveolar lavage fluid were measured by ELISA. Samples of bronchoalveolar lavage fluid and mediastinal lymph nodes were harvested from each group of mice and subjected to flow cytometric analysis for quantification of the relevant immune cell populations.

2.8. Biosafety assessment

To evaluate the biotoxicity of RL-NE@Man on normal bronchial epithelial cells, BEAS-2B cells were incubated with various concentrations of RL-NE@Man (0, 0.1, 0.3, 0.5, 1.0, 1.5, 2.0, 5.0 and 10.0 μmol/L). After 48 h, cell viability was assessed using the standard CCK-8 assay. For *in vivo* biosafety evaluation, healthy mice were administered high concentrations of RL-NE@Man (10 mg/kg) *via* nebulized inhalation. Body weight was monitored in the RL-NE@Man-administered mice, with the PBS-treated group serving as the control. On Day 3 post-administration, blood samples were collected for hematological parameter analysis and serum biochemical assays. Major organs (heart, liver, spleen, lung, and kidney) were harvested from euthanized mice and subjected to tissue sectioning and H&E staining.

2.9. Statistical analysis

All the data were analyzed using GraphPad Prism 10, except for those in Supporting Information Table S1 and Fig. S2B, which were generated by Design-Expert 12. Colocalization analysis was performed using ZEN software. For comparisons between two groups, two-tailed unpaired Student's *t*-tests were used. Multiple group comparisons were analyzed by one-way ANOVA. The data are presented as the mean ± standard deviation (SD). Statistical significance was set at $P < 0.05$, with the following thresholds: $P < 0.05$ (*), $P < 0.01$ (**), $P < 0.001$ (***), and $P < 0.0001$ (****).

3. Results

3.1. Preparation and characterization of RL-NE@Man

Considering the future large-scale production and translational potential of the prepared nebulized inhalation agents, we selected soybean oil and DPPC, both of which are approved by the FDA, as the primary delivery materials. The nanoemulsion was prepared by the high-pressure homogenization method, as shown in Fig. 1A. The Box−Behnken design (BBD) method was utilized to optimize the preparation process of the nanoemulsion, with drug loading capacity and particle size serving as the primary evaluation criteria (Fig. 1B and Supporting Information Table S1). The small particle size of inhaled nanoparticles facilitates their deposition in deep pulmonary regions[31]. The particle size and zeta potential of the final RL-NE screened by dynamic light scattering were 108.1 ± 1.5 nm and -8.4 ± 2.03 mV, respectively (Fig. 1C). Compared with the RL-NE, the mannosylated nanoemulsion RL-NE@Man had a slightly larger (123.0 ± 2.2 nm) particle size (Fig. 1D). The appearance of the RL-NE@Man remained clear without noticeable sedimentation or layering during storage at 4 °C for 3 months (Fig. 1E). The hydrodynamic sizes of both nanoparticles ranged between 100 and 150 nm, with comparable polydispersity indices (PDI) in the range of 0.1 ∼ 0.2 (Fig. 1F and G), which fall within an acceptable range and indicate good storage stability of the nanoemulsion. The *in vitro* release behavior of rifampicin and LCL161 was further measured by HPLC in phosphate buffered saline (PBS) supplemented with 10% serum and 1% sodium dodecyl sulfate. The results revealed that RL-NE@Man released 63.2% of rifampicin (Supporting Information Fig. S1A) and 54.7% of LCL161 (Fig. S1B) within 24 h, and a sustained-release behavior was observed within 72 h. To achieve long-term storage of RL-NE@Man, we investigated the optimal addition ratios of three approved cryoprotectants (sucrose, mannitol, and trehalose), which can be used as excipients for inhalable formulations. The results revealed that only the freeze-

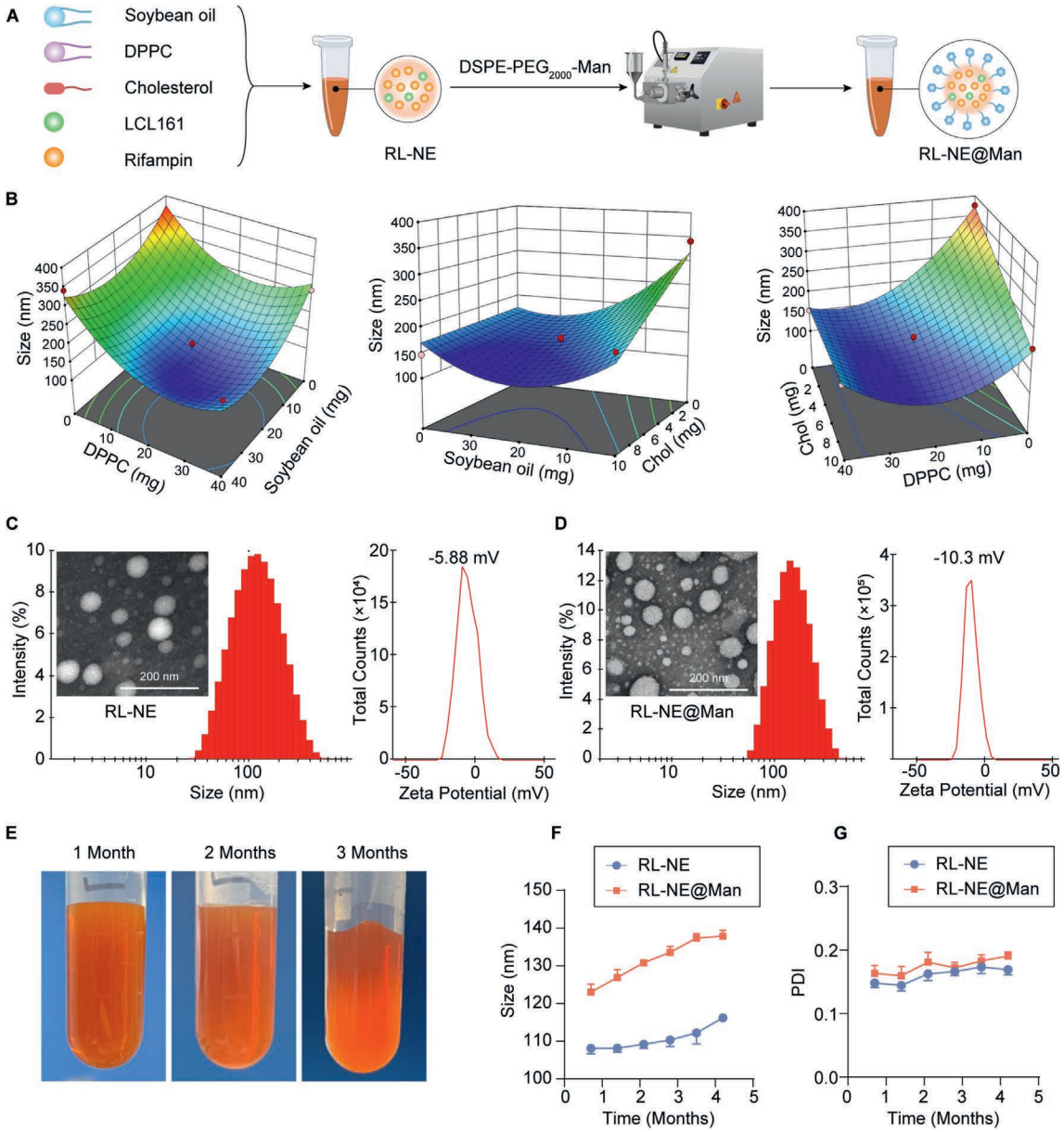

Figure 1 Preparation and characterization of RL-NE@Man. (A) Schematic diagram of the preparation process of RL-NE and RL-NE@Man. (B) The formulation of the nanoemulsion was optimized using response surface design *via* Design-Expert 12 software. (C, D) Physicochemical characterization of RL-NE (C) and RL-NE@Man (D), showing the hydrodynamic size distribution, zeta potential, and a representative TEM image for each formulation. (E) Visual observation of RL-NE@Man after 3 months of storage at 4 °C. (F, G) The particle size (F) and PDI (G) of RL-NE and RL-NE@Man during *in vitro* storage at 4 °C ($n = 3$). The data are presented as the mean ± SD.

dried formulation containing 10% trehalose in the emulsion exhibited minimal changes in particle size and PDI upon reconstitution (Supporting Information Table S2), thereby enabling the long-term storage of the RL-NE@Man (Fig. S1C).

3.2. RL-NE@Man exhibits excellent nebulization and inhalation performance

The nebulization performance of inhalation formulations is influenced by multiple factors, including the type of nebulizer, drug concentration in the formulation, viscosity of the liquid, and physicochemical properties of the formulation. On the basis of previously published study[32], we utilized a next generation impactor (NGI) to evaluate the size and aerodynamic performance of the RL-NE@Man before and after nebulization. The NGI is a commonly used instrument for evaluating the aerodynamic particle size distribution of aerosol inhalation products[33,34]. By simulating the human respiratory tract, the deposition of aerosol particles at different stages of the airways can be measured, providing critical data for assessing the performance of inhalation drug delivery systems (Fig. 2A). An atomizing inhaler (PARI BOY SX, Germany) has been widely used in clinical practice for atomization (Fig. 2B). To test whether the stability of RL-NE@Man is affected after nebulization, nebulized RL-NE@Man was collected separately using a PARI BOY SX and a microspray nebulization device (BJ-PW-R; BioJane, China). The

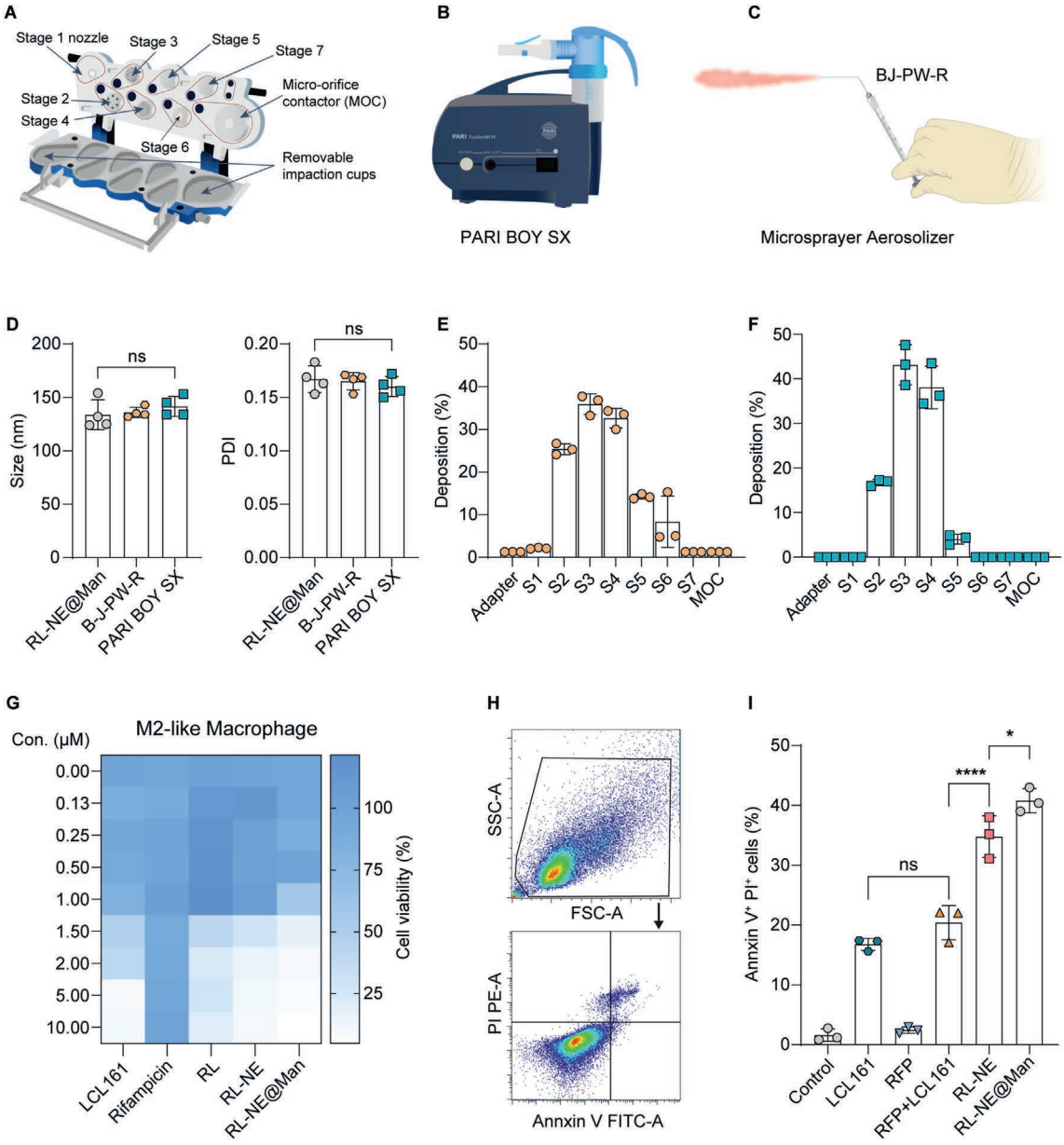

Figure 2 Aerosol inhalation performance analysis of RL-NE@Man. (A) The aerosol inhalation performance of RL-NE@Man was evaluated using the NGI to simulate real breathing. (B) Aerodynamic characterization nebulizer: PARI BOY SX. (C) Precise and quantitative nebulization administration in mice using a microsprayer aerosolizer. (D) Investigation of the size and PDI of RL-NE@Man after nebulization with two nebulizers ($n = 4$). (E, F) Aerial particle size distributions of rifampicin (E) and LCL161 (F) ($n = 3$). (G) A CCK-8 assay was performed to evaluate the cytotoxicity of M2-like macrophages following distinct treatment regimens ($n = 6$). (H, I) Flow cytometric gating strategy and quantitative analysis (I) of apoptotic cell counts in M2-like macrophages ($n = 3$). The data are presented as the mean ± SD. Statistical analysis was performed by one-way ANOVA. $^*P < 0.05$, $^{****}P < 0.0001$. ns, not significant. M, mol/L.

microsprayer is a device designed for the quantitative delivery of aerosols to small animals and has been employed in numerous studies[35,36] (Fig. 2C). The results shown in Fig. 2D demonstrated that the morphology (Supporting Information Fig. S2), particle size, and PDI of RL-NE@Man were not significantly affected after aerosolization using either a PARI BOY or a microspray nebulizer. The aerodynamic performance results of RL-NE@Man indicated that RL-NE@Man exhibits favorable drug deposition in stages 2 to 6, suggesting that the cutoff diameter of RL-NE@Man post-inhalation falls within the range of 3 to 5 μm (Fig. 2E and F, Supporting Information Table S3). The 1−5 μm particle size range is optimal for pulmonary delivery, minimizing exhalation (<0.5 μm) and oropharyngeal deposition (>5 μm). Triplicate experiments demonstrated that RL-NE@Man exhibited excellent aerosolization performance, with mean fine particle fractions (FPF) of 42.64% and 32.40% for rifampicin and LCL161, respectively, and geometric standard deviations (GSD) below 1.5, indicating favorable characteristics for enhanced pulmonary drug deposition (Supporting Information Table S3). Furthermore, we systematically evaluated the cytotoxicity and apoptosis-inducing

capacity of the nanoemulsion against M2 macrophages. As shown in Fig. 2G, compared with free LCL161, rifampicin was not cytotoxic to M2 macrophages at 0−10 μmol/L, whereas RL-NE@Man achieved a significantly lower IC_{50} (1.09 μmol/L, half of that of the RL-NE group). RL-NE@Man had the most potent apoptotic effect on M2 macrophages (Fig. 2H and I, Supporting Information Fig. S3).

3.3. The nanoemulsion demonstrates exceptional in vitro antibacterial activity

We next evaluated the *in vitro* antibacterial activity of RL-NE@Man. In resazurin assays, optical density measurements, and colony formation assays, RL-NE@Man and RL-NE exhibited comparable antimicrobial activity and consistently outperformed the other treatments (Fig. 3A and B, Supporting Information Fig. S4). Notably, all the results indicated that the blank nanoemulsion (NE, devoid of active drugs) also contributed to antibacterial activity, with its concentration calculated on the basis of the mass of excipients specified in the formulation. We hypothesize that this phenomenon may be attributed to the unsaturated fatty acids incorporated into our formulation. Extensive studies have demonstrated that unsaturated fatty acids exhibit antimicrobial effects through multiple mechanisms, such as disrupting bacterial cell wall integrity, inhibiting fatty acid synthesis, and suppressing biofilm formation[37-39]. Furthermore, by scanning electron microscopy, we directly observed that the *M. tuberculosis* treated with RL-NE@Man exhibited more disintegration and breakage than the control bacteria did (Fig. 3C). Since *M. tuberculosis* is a classic intracellular pathogen, we conducted cellular uptake experiments with a nanoemulsion to validate the intracellular delivery efficiency of the antibiotic-loaded nanoemulsions. Flow cytometry analysis revealed that compared with the M2 macrophages in the RL-NE group, the M2 macrophages in the RL-NE@Man group exhibited a 1.74-fold greater uptake intensity (Fig. 3D). *M. tuberculosis* infection induced the dual polarization of BMDMs into both M1 and M2 phenotypes after 72 h of exposure, and the M2 macrophages markedly decreased in the RL-NE@Man group, reaching only 43.5% of those in the RL-NE group and 16.6% of those in the *M. tuberculosis* group (Fig. 3E). Notably, compared with M1 BMDMs, H37Ra-infected BMDMs (*Mtb*) exhibited more pronounced polarization toward the M2 phenotype. Furthermore, none of the drug treatments significantly altered the proportion of M1 macrophages (Fig. 3F). These results demonstrated that RL-NE@Man selectively reduced the proportion of M2 macrophages known to protect tuberculosis growth while preserving M1 macrophages that possess anti-tuberculosis activity.

3.4. Investigation of the effects of RL-NE@Man on the transcriptional profiles and phenotypic alterations in M. tuberculosis-infected macrophages

To investigate the impact of *M. tuberculosis* on macrophages, *M. tuberculosis* was cocultured with BMDMs for different durations. Following stimulation with the H37Ra strain, the cells exhibited cellular swelling, pseudopod formation, and the development of foamy macrophages (Fig. 4A). After 12 h, the BMDMs were collected for transcriptomic analysis. Compared with the cell infection model group, the nanoemulsion intervention group had significantly upregulated expression of 410 genes and downregulated expression of 1525 genes (Fig. 4B and C). A total of 1447 genes were significantly involved in the three different treatment groups (Fig. 4D). Kyoto Encyclopedia of Genes and Genomes (KEGG) pathway enrichment analysis revealed that *M. tuberculosis*-stimulated BMDMs were enriched in pathways associated with TB (red), pattern recognition receptors (PRRs; orange), and inflammation (blue) (Fig. 4E). *M. tuberculosis*-infected BMDMs in the *Mtb* group showed an upregulated expression of genes associated with proinflammatory cytokines, chemokines and macrophage polarization, and that intervention with the drug RL-NE@Man (NM) resulted in a reduction in the levels of several proinflammatory and chemokine factors and prevented excessive inflammatory responses (Fig. 4F). In particular, the expression of M2 macrophage-associated genes such as *Egr2*, *Arg1*, and *IL-10* was significantly upregulated. However, these genes were downregulated following RL-NE@Man intervention (Fig. 4G), while M1 macrophage-associated genes such as *Gpr18* and *iNOS* remained unaffected (Fig. 4H). These findings align with the macrophage phenotypic alterations observed in Fig. 3F.

3.5. RL-NE@Man exhibits significant retention in lung tissue and achieves targeted delivery to tuberculosis granulomas

To investigate the *in vivo* distribution of RL-NE@Man after inhalation in tuberculosis-infected mice, we first established a mouse model of infection with *M. tuberculosis* (Fig. 5A). Histological, immunohistochemical, and acid-fast staining analyses collectively confirmed the establishment of a well-defined tuberculous granuloma mouse model (Fig. 5B, and Supporting Information Fig. S5), consistent with established pathological features reported in the literature[23]. Mice were administered the fluorescent dye DID-labeled RL-NE@Man *via* tail vein injection and a microsprayer aerosolizer. The fluorescence signals were detected using a small-animal *in vivo* imaging system (IVIS). The results shown in Fig. 5C indicate that direct pulmonary administration *via* nebulization significantly reduces drug distribution in other organs compared with intravenous injection, with the highest drug exposure observed in lung tissues. To further determine the extent of the distribution of RL-NE@Man within the pulmonary lobes, we dissected the lungs into their five constituent lobes and observed uniform luminescence across all of them (Fig. 5D). Importantly, compared with that in the intravenous injection group, the fluorescence retention signal in the RL-NE@Man group was significantly stronger following inhalation. We monitored the distribution of fluorescent signals in the major organs of the mice at three time points following the nebulization administration of RL-NE@Man (Fig. 5E). The semiquantitative results at 24 h post-administration revealed that RL-NE@Man treatment significantly increased the intensity of fluorescent signals in the lung tissues of the mice (Fig. 5F). Immunofluorescence analysis revealed significantly stronger green fluorescence intensity (coumarin-6-loaded nanoemulsion) in RL-NE@Man-treated lung tissues than in RL-NE control lung tissues (Fig. 5G and H). The signal strongly colocalized with that of $CD206^+$ macrophages, which are key reservoirs of *M. tuberculosis*. Furthermore, we observed that both nanoemulsion groups were able to target the granuloma structures (Fig. 5I). Compared with the RL-NE group, the RL-NE@Man group exhibited stronger colocalization with *M. tuberculosis* in the lung tissues of the mice (Fig. 5J). These findings suggest that RL-NE@Man could further increase the intracellular drug concentration within *M. tuberculosis*-infected macrophages. Combined with the *in vitro* cellular uptake data,

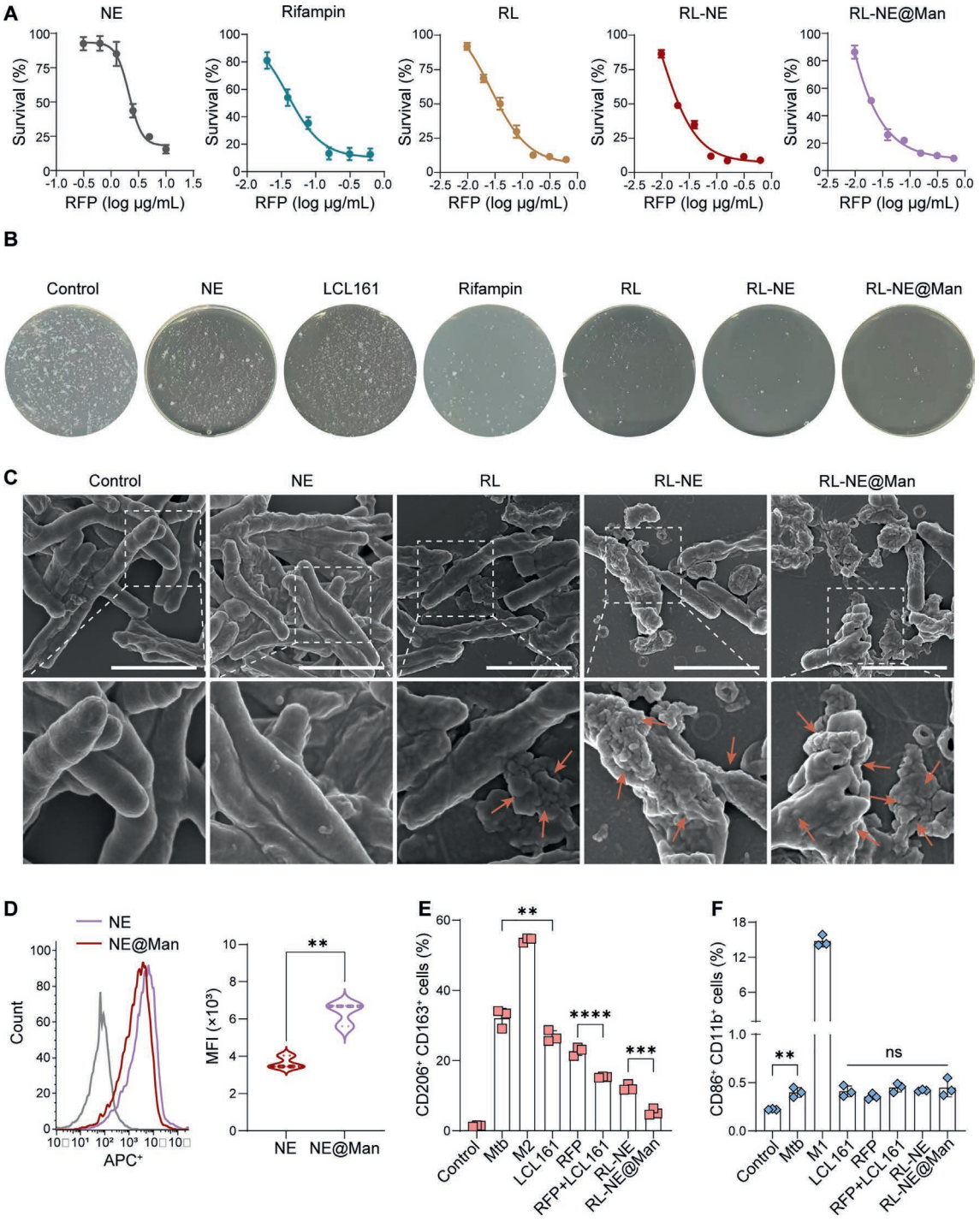

Figure 3 Multidimensional evaluation of the *in vitro* antibacterial activity of RL-NE@Man. (A) The resazurin method was used to investigate the survival rate of H37Ra bacilli treated with different nanoemulsions ($n = 6$). The *x*-axis for NE represents the administered volume, which is based on equivalent rifampicin volumes. (B) Representative images showing the growth of *M. tuberculosis* colonies following treatment. (C) Representative SEM images of H37Ra bacilli after 3 days of coincubation with different nanoemulsions. The arrows indicate the shrinkage and rupture of the bacteria. Scale bars, 2 μm. (D) Flow cytometry was used to analyze the intensity of the uptake of DID-labeled NE@Man by M2 macrophages ($n = 3$). (E, F) Proportion of M2 (E) and M1 (F) macrophages in *M. tuberculosis*-infected BMDMs under different treatments, as determined by flow cytometry ($n = 3$). The data are shown as the mean ± SD. Statistical analysis was performed by one-way ANOVA. $^{**}P < 0.01$, $^{***}P < 0.001$, and $^{****}P < 0.0001$. ns, not significant.

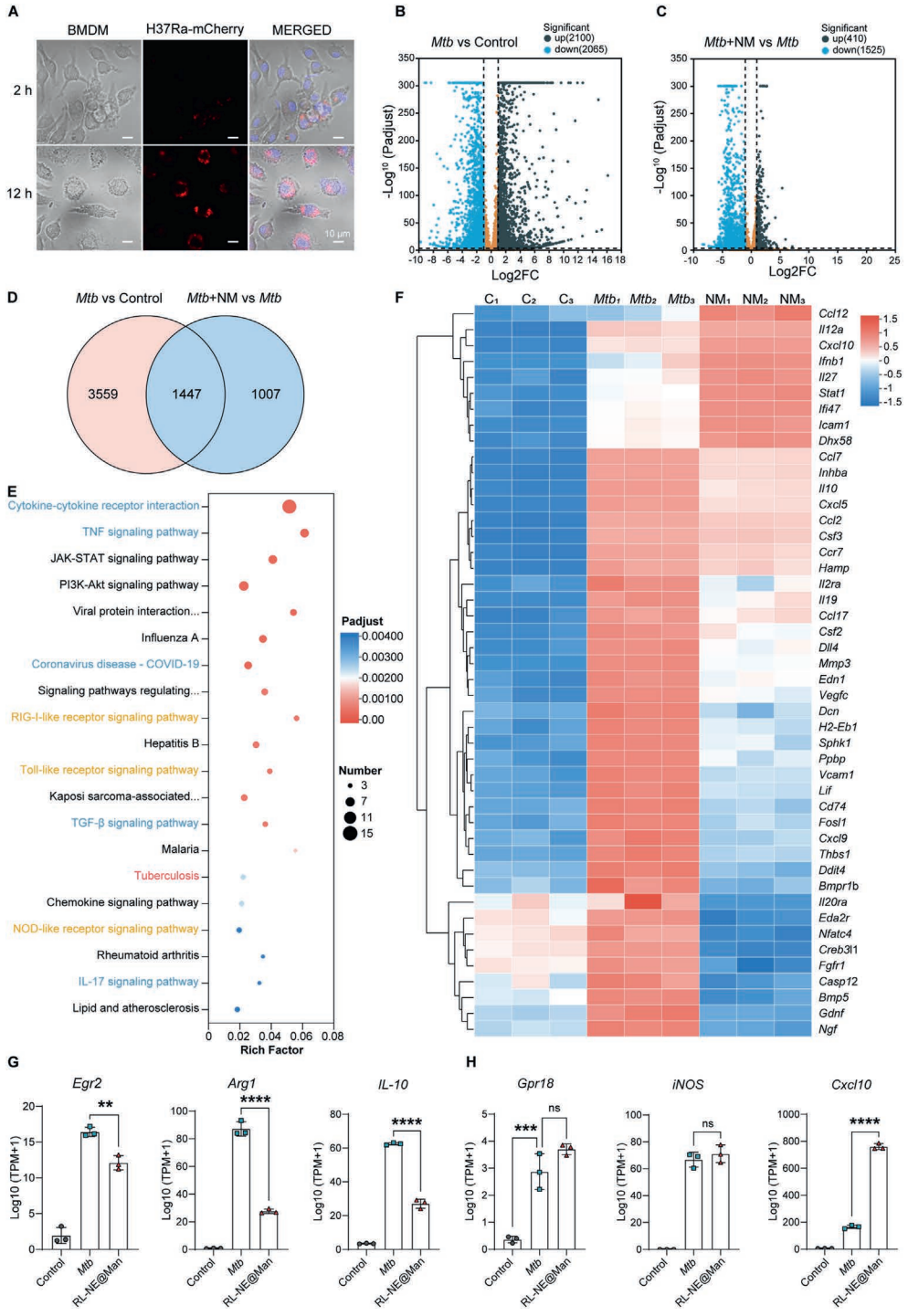

Figure 4 Transcriptomic and phenotypic analysis of BMDMs cocultured with H37Ra bacilli under different nanoemulsion interventions. (A) Changes in the morphology of BMDMs after coculture with *M. tuberculosis* H37Ra-mCherry at 37 °C for different durations. Scale bar, 10 μm. (B) Analysis of differentially expressed genes (DEGs) between the *Mtb* and control groups (named C). (C) DEGs between the *Mtb* + RL-NE@Man (denoted as NM) group and the *Mtb* group. (D) Venn analysis of all DEGs in H37Ra bacilli treated with control or *Mtb* + NM. (E) KEGG pathway enrichment analysis of transcriptomic data from macrophages treated with *Mtb* or NM for 12 h, focusing on bacterial infection and immune responses. (F) Visualization of the corresponding differentially expressed genes in a heatmap (fold change >2 and $P < 0.001$). (G) The expression of the M2 macrophage marker genes *Egr2*, *Arg1*, and *IL-10*. (H) The expression of the M1 macrophage marker genes *Gpr18*, *iNOS*, and *Cxcl10*. The data are presented as the mean ± SD, $n = 3$. Statistical analysis was performed by one-way ANOVA. $^{**}P < 0.01$, $^{***}P < 0.001$, and $^{****}P < 0.0001$. ns, not significant.

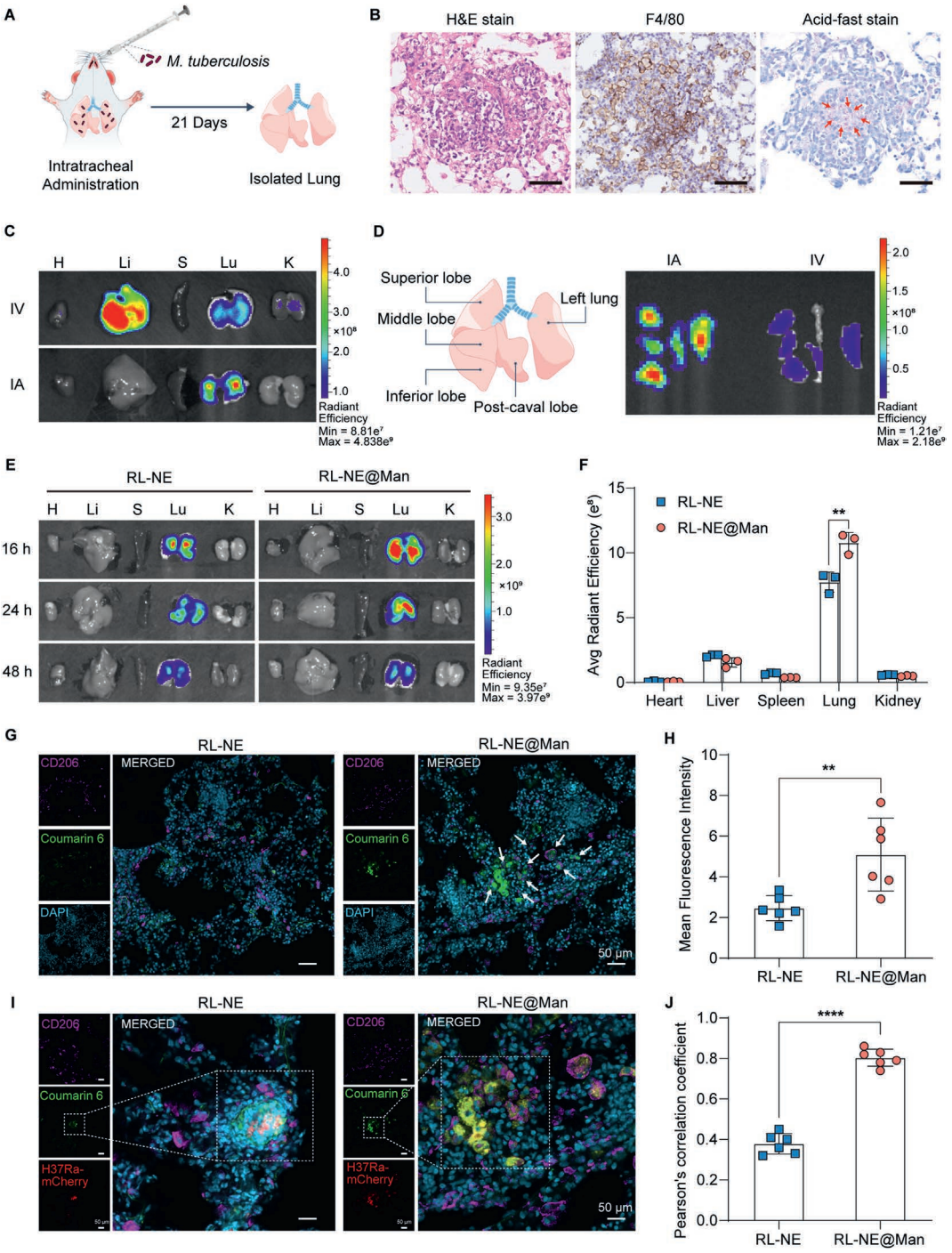

Figure 5 *In vivo* distribution of RL-NE@Man after inhalation in mice. (A) C57BL/6 mice were aerosol-infected with *Mtb* H37Ra *via* a micronebulizer, and the lungs were harvested 21 days post-infection. (B) Histopathology (H&E, F4-80 immunohistochemistry, acid-fast staining) of lung tuberculous granulomas in H37Ra-induced TB mice. Scale bar = 50 μm. (C) Comparison of nanoemulsion tissue distribution between intravenous (IV) and aerosol inhalation (IA) administration in mice. (D) Distribution of nanoemulsions in different lung lobes of mice. (E) IVIS imaging of the time-dependent biodistribution of RL-NE@Man in mice postinhalation ($n = 3$). (F) Semiquantification of organ fluorescence in mice 24 h after aerosol treatment ($n = 3$). (G) Murine lung immunofluorescence 24 h postinhalation was used to assess the pulmonary distribution of the coumarin 6-labeled nanoemulsion (green). (H) Semiquantitative analysis of Coumarin 6 in six random fields using Zeiss ZEN software. (I) Immunofluorescence staining of murine lung tissues was conducted 24 h after aerosol administration. Representative immunofluorescence image of lung tissues showing a coumarin 6-labeled nanoemulsion (green) with CD206 (purple, M2 macrophage marker), and DAPI (blue, nuclear). Scale bar = 50 μm. (J) Quantitative analysis of the colocalization of coumarin 6 and H37Ra-mCherry in six random fields using Pearson's correlation coefficient (PCC >0.5 considered significant). The data are presented as the mean ± SD. Statistical analysis was performed by one-way ANOVA. $^{**}P < 0.01$, $^{****}P < 0.0001$.

these results substantiate our hypothesis that our meticulously engineered RL-NE@Man can reach pulmonary tuberculous granuloma sites through inhalation and increase the efficiency of nanoemulsion cellular internalization *via* specific interactions with mannose receptors (CD206) on macrophages.

3.6. In vivo anti-TB effects

To evaluate the antituberculosis therapeutic efficacy of nebulized RL-NE@Man, we established a mouse model of infection with *M. tuberculosis* H37Ra and initiated treatment on the 22nd day after infection. After two treatment sessions, we collected and analyzed relevant indicators on the 36th day (Fig. 6A). H&E staining revealed marked infiltration of granulocytes, lymphocytes, and macrophages within the alveolar walls, along with disrupted alveolar architecture, in the PBS group. These pathological features were moderately alleviated in both the free RFP and RFP + LCL161 treatment groups (Fig. 6B). Compared with the RL-NE-treated mice, the RL-NE@Man-treated mice exhibited significantly attenuated inflammatory infiltration, reduced granulomatous lesions, and a well-preserved bronchial architecture with an intact structural hierarchy in pulmonary tissues (Fig. 6B). The acid-fast staining results for the mouse lung tissues revealed that the antibacterial effect of RL-NE@Man was significantly superior to that of the other treatment groups (Fig. 6C). Furthermore, compared with the other groups, the RL-NE@Man group presented the lowest number of F4/80-positive macrophages in the lung tissues (Fig. 6D).

Flow cytometry demonstrated that compared with control mice, mice treated with RL-NE@Man exhibited the highest degree of dendritic cell maturation and expression of MHC class II molecules in the mediastinal lymph nodes (Fig. 6E and F, Supporting Information Fig. S6). Moreover, in the mediastinal lymph nodes, the RL-NE@Man treatment resulted in the lowest percentage of M2 macrophages. Concurrently, it promoted M1 macrophage polarization, achieving percentages that were 1.49-fold and 3.47-fold greater than those in the RL-NE and RFP groups, respectively (Supporting Information Figs. S7 and S8). RL-NE@Man treatment induced the most significant reduction in the M2 macrophage population in the BALF (Fig. 6G). In contrast, no significant difference in the number of M1 macrophages was detected among the groups (Fig. 6H). This phenotypic shift in macrophages is consistent with the results observed *in vitro* (Fig. 3E and F). Concurrently, the population of immunosuppressive M2-like macrophages and their associated protein markers (*e.g.*, CD206 and SPP1) were significantly reduced (Supporting Information Fig. S9). RL-NE@Man treatment significantly reduced the numbers of neutrophils (Fig. 6I) and myeloid-derived suppressor cells (MDSCs) (Fig. 6J and Supporting Information Fig. S10) in the BALF of mice. Similarly, the RL-NE@Man group exhibited the most substantial expansion of both $CD4^+$ and $CD8^+$ T-cell populations in the lymph nodes (Supporting Information Fig. S11), suggesting that the elimination of immunosuppressive M2 macrophages and MDSCs enhanced antibacterial immunity. Notably, compared with those in the control group, the bacterial clearance efficacy in the RL-NE@Man inhalation therapy group was 94.5% lower in pulmonary *M. tuberculosis Ag85b* expression (qPCR), with the bacterial clearance efficacy surpassing that in the RL-NE treatment group (Fig. 6K). Moreover, at the molecular level, the levels of TNF-α, IL-6, and IFN-γ in the bronchoalveolar lavage fluid in the RL-NE@Man group were reduced by 51.22%, 60.49%, and 67.1%, respectively, compared with those in the control group (Fig. 6L and Supporting Information Fig. S12). The levels of these inflammatory cytokines are closely associated with the prognosis of pulmonary tuberculosis. Immunohistochemical analysis of TNF-α, IL-6, and IL-1β expression in murine lung tissues yielded concordant results (Supporting Information Fig. S13), further validating the enhanced therapeutic efficacy of RL-NE@Man over RL-NE and free drug controls in attenuating granulomatous pathology.

3.7. Biotoxicity evaluation

Finally, we evaluated the biotoxicity of RL-NE@Man *in vitro* and *in vivo*. The evaluation commenced at the cellular level, where the potential for direct cytotoxicity was assessed using BEAS-2B normal human lung epithelial cells. This cell line was selected as it represents the primary physiological barrier that an inhaled therapeutic would encounter. Cells were exposed to a broad spectrum of RL-NE@Man concentrations for a prolonged duration of 48 h, a timeframe designed to uncover any latent or delayed cytotoxic effects. Reassuringly, subsequent cell proliferation assays revealed only a minimal, concentration-independent suppression of growth. Even at the highest concentrations tested, the viability of BEAS-2B cells remained largely unaffected, indicating a negligible cytotoxic footprint and underscoring the innate biocompatibility of the nanoemulsion formulation (Fig. 7A). Building upon these promising *in vitro* results, we proceeded to evaluate systemic tolerance in a living organism. Mice were subjected to repeated nebulization of RL-NE@Man, mimicking the intended route of administration. Systemic health was meticulously monitored, with body weight serving as a primary and sensitive indicator of overall well-being and acute toxicity. Over the course of the observation period, all animal cohorts maintained stable and normal growth trajectories, with no group exhibiting any significant weight loss compared to the vehicle-control group. This absence of gross physiological disturbance strongly suggests that the nanoemulsion is well-tolerated and does not induce acute systemic toxicity (Fig. 7B). To obtain a deeper, histopathological perspective, a comprehensive analysis was performed on the third day after administration. At this timepoint, blood samples were collected for hematological and biochemical profiling, and major organs-including the heart, liver, spleen, lungs, and kidneys-were harvested for detailed examination. Histological evaluation of tissue sections *via* H&E staining provided a microscopic view of organ integrity. Critically, this analysis uncovered no evidence of pathological alterations across any of the organs inspected. The tissue architecture remained pristine, with no signs of necrosis, apoptosis, cellular vacuolization, or abnormal inflammatory cell infiltration (Fig. 7C). The nanoemulsion left no discernible mark on the vital organ structures. Finally, the collected blood samples were subjected to detailed analysis. Routine blood index analysis, which assesses the health of the hematopoietic system, showed that all key parameters-including red blood cells, white blood cells, and platelets-remained within normal physiological ranges following RL-NE@Man treatment (Supporting Information Fig. S14A). Concurrently, plasma biochemistry panels, which are critical for evaluating liver function and kidney function, confirmed the absence of organ damage. All measured indicators were unaltered compared to control groups (Fig. S14B). Together, these data provide compelling evidence that RL-NE@Man induces no acute damage to the vital hematopoietic, hepatic, or renal systems. In

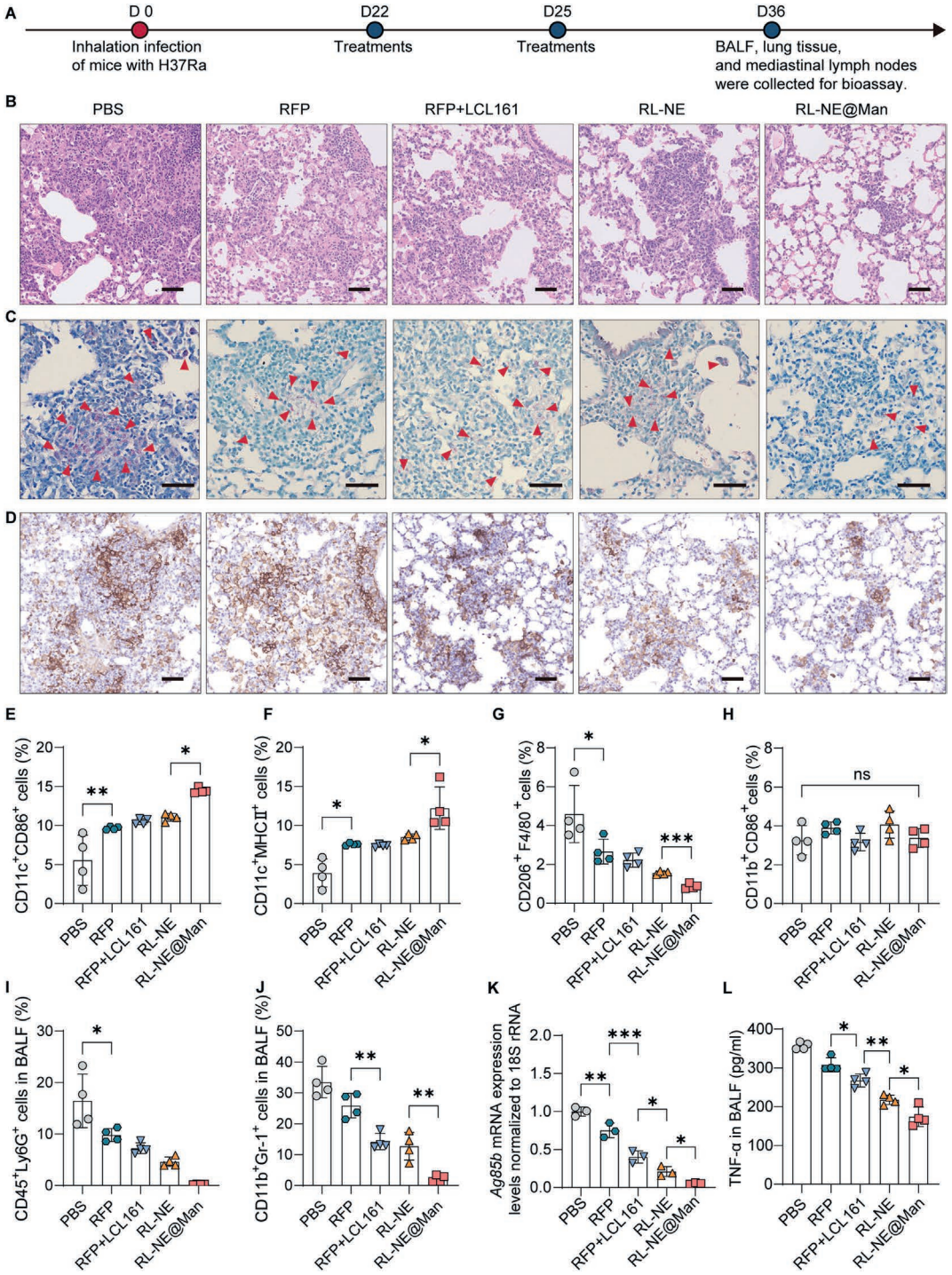

Figure 6 Evaluation of the antibacterial and anti-inflammatory therapeutic efficacy of RL-NE@Man against H37Ra-induced pulmonary tuberculosis in mice. (A) Schematic timeline of H37Ra-induced murine tuberculosis model development, therapeutic intervention, and experimental sampling procedures. (B) H&E staining of lung tissues sections after different treatments. (C) Acid-fast staining of murine lung tissues across different treatment groups. Red triangles indicate *M. tuberculosis*. (D) Immunohistochemistry for F4/80 (macrophage marker). Scale bar = 50 μm. Representative images from three independent experiments with consistent results are shown. (E) Dendritic cell maturation in the mediastinal lymph nodes ($n = 4$). (F) Expression levels of MHC class II molecules on dendritic cells from the mediastinal lymph nodes ($n = 4$). (G) The proportion of M2 macrophages in the BALF ($n = 4$). (H) The proportion of M1 macrophages in the BALF ($n = 4$). (I) The proportion of neutrophils in the BALF as detected by flow cytometry ($n = 4$). (J) The percentage of MDSCs in the BALF, quantified by flow cytometry ($n = 4$). (K) qPCR detection of *M. tuberculosis Ag85b* DNA in lung homogenates ($n = 3$). (L) Comparison of the levels of the pro-inflammatory cytokine TNF-α in the BALF of tuberculosis-infected mice following the designated treatment ($n = 4$). For panels E-L, data are presented as the mean ± SD. Statistical analysis was performed by one-way ANOVA. $^*P < 0.05$, $^{**}P < 0.01$, $^{***}P < 0.001$. ns, not significant.

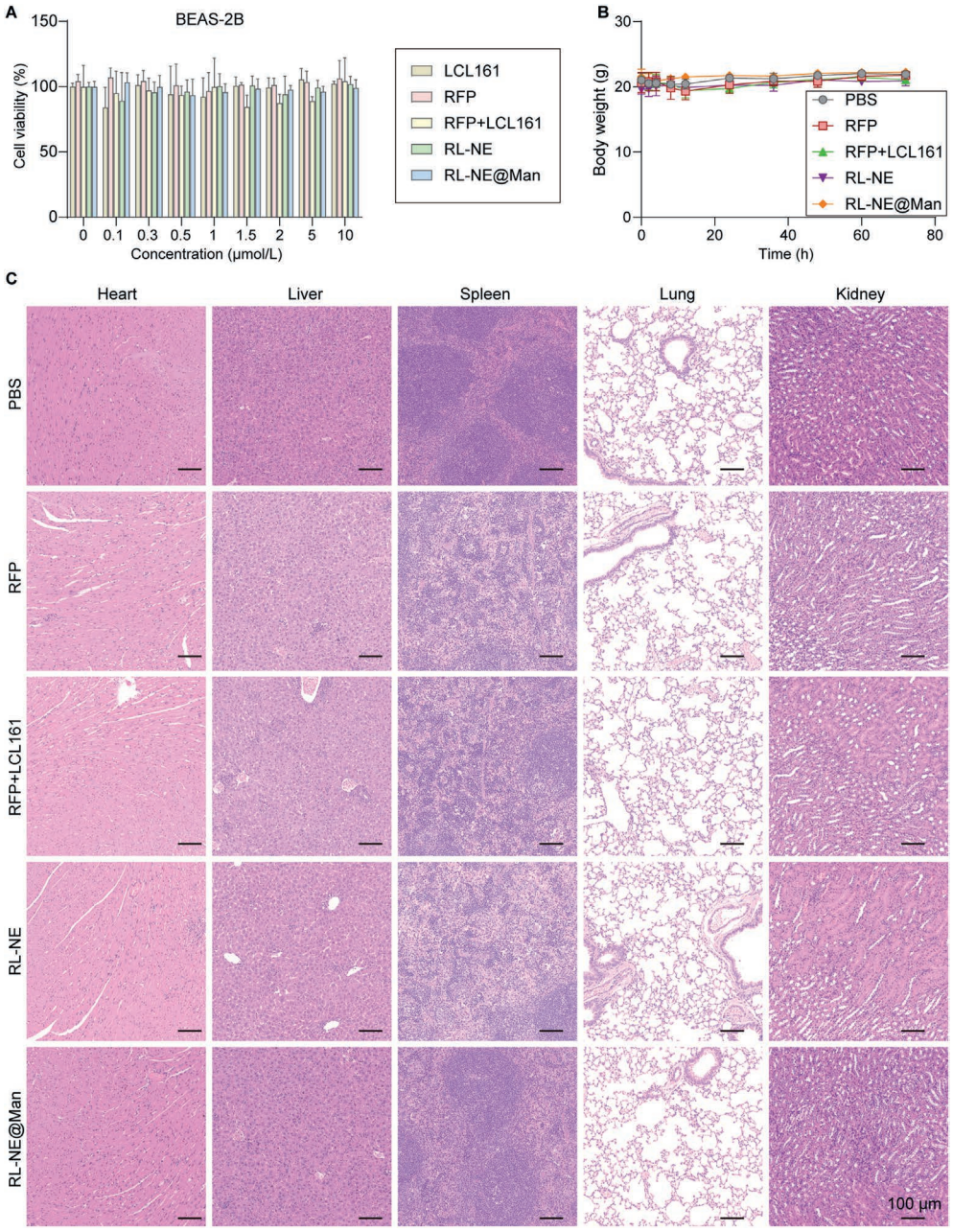

Figure 7 Safety evaluation of RL-NE@Man following aerosol inhalation. (A) CCK-8 assay-based evaluation of proliferative activity in BEAS-2B cells in different groups treated for 48 h ($n = 5$). (B) Time-course body weight curve of mice following two aerosol administrations ($n = 3$). (C) H&E staining of major organs. Scale bar = 100 μm. Data are expressed as mean ± SD.

summary, through a coordinated series of experiments from the cellular to the whole-organism level, we have robustly established that RL-NE@Man exhibits an outstanding safety profile. Its minimal cytotoxicity, excellent *in vivo* tolerance, and absence of histopathological or hematological abnormalities strongly advocate for its further development as a promising and safe inhaled therapeutic agent against pulmonary infections.

4. Discussion

The treatment of tuberculosis caused by *M. tuberculosis* infection remains a formidable challenge, as conventional antibiotics suffer from low bioavailability, inadequate targeting, and limited therapeutic efficacy. Prolonged antibiotic use further leads to poor patient compliance and may even contribute to the development of multidrug-resistant tuberculosis. The host immune response serves as a critical determinant of tuberculosis containment; however, the pathogen *M. tuberculosis* demonstrates persistent survival under active immune surveillance.

Previous studies have reported that following phagocytosis by macrophages *via* the respiratory tract, *M. tuberculosis* employs lipid constituents of its cell wall to suppress phagosome−lysosome fusion and modulate host immune responses, thereby facilitating its long-term intracellular survival within macrophages[40,41]. Given the host infection characteristics

of *M. tuberculosis* and the histopathological features of tuberculous granulomas, conventional antibiotics struggle to achieve effective therapeutic concentrations at the lesion site through intravenous or oral administration. The advancement of nanomaterials offers a novel perspective for addressing the limitations of conventional antibiotics and improving tuberculosis treatment efficacy.

Study has identified immunomodulatory nanoparticles that mitigate pulmonary *M. tuberculosis* burden in murine models through the induction of macrophage autophagy[42], which creates a therapeutic opportunity to recalibrate antimicrobial responses in the tuberculous niche through targeted orchestration of macrophage polarization toward a microbiocidal phenotype[43]. A recent study demonstrated that intravenously administered nanoparticles capable of dual targeting tuberculous granulomas and intracellular *M. tuberculosis* could eradicate the pathogen through photothermal effects. This nanotherapeutic approach outperformed first-line antibiotic regimens by simultaneously mitigating pulmonary pathology and excessive inflammation[23]. However, these nanoparticles face significant translational challenges, including complex fabrication processes, high production costs, and limited scalability for industrial manufacturing. Previous study has demonstrated that clinical-stage compounds can antagonize inhibitor of apoptosis proteins to target apoptotic pathways, thereby enhancing *M. tuberculosis* clearance in murine models[19]. However, significant challenges remain exist, including high dosage requirements, severe toxicity risks, and a lack of comprehensive evaluation regarding their therapeutic efficacy when combined with first-line antibiotics.

In this study, we report a rationally integrated, host-directed therapeutic platform that utilizes an inhalable biomimetic nanoemulsion co-loaded with rifampicin and LCL161, synergizing the strengths of existing modalities while incorporating systematic engineering to overcome their inherent limitations. This system has demonstrated the ability to induce apoptosis in infected macrophages, promote clearance of *M. tuberculosis*, and modulate immune responses within the tuberculous microenvironment in murine models. RL-NE@Man demonstrates superior anti-tuberculosis efficacy through multiple mechanisms. First, the RL-NE@Man system exhibits optimal aerodynamic properties for pulmonary delivery, enabling enhanced penetration and retention in tuberculosis-infected murine models. It achieves mannose receptor-mediated targeting of *M. tuberculosis*-infected macrophages while demonstrating precise co-localization with intracellular pathogens (Fig. 5G and I). Second, *in vitro* antibacterial efficacy evaluations revealed that free LCL161 alone did not exhibit significant antimycobacterial activity (Fig. 3B and Fig. S4); notably, the blank nanoemulsion formulation displayed measurable antibacterial activity, which may have arisen from the inherent antimicrobial properties of the unsaturated fatty acids present in its excipient composition (Fig. 3A−C and Fig. S4). Furthermore, in murine tuberculosis models, RL-NE@Man inhalation therapy significantly modulated adaptive immunity by enhancing M1 macrophage polarization while suppressing M2 phenotype in mediastinal lymph nodes of mice (Fig. S7), concurrently expanding both $CD4^+$ and $CD8^+$ T cell populations (Fig. S11). These findings align with established reports demonstrating that apoptosis of *M. tuberculosis*-infected macrophages contributes to the generation of antigen-specific T cell responses[44,45]. Moreover, the reduced bacterial burden in lung tissues (Fig. 6K) contributed to the concomitant attenuation of pro-inflammatory cytokines (IL-6, TNF-α, and IFN-γ), which are established biomarkers of disease severity and mycobacterial burden[46,47]. This anti-inflammatory effect aligns with clinical observations of decreased plasma cytokine levels during therapeutic interventions[46,48]. Notably, we developed a lyophilization-stable nanoemulsion formulation using scalable emulsification techniques. The formulation parameters were systematically optimized through a Box−Behnken experimental design to ensure long-term storage stability. Critical inhalation quality parameters were systematically optimized through both formulation composition refinement and aerodynamic performance enhancement.

Our study has several limitations. While our study successfully demonstrated effective modulation of the tuberculous microenvironment in murine models, with significant reductions in pulmonary bacterial burden and enhanced safety profiles, these findings remain to be validated in non-human primates. Although nanotechnology-enhanced antibiotics and immunomodulators have demonstrated remarkable therapeutic efficacy in overcoming bacterial resistance, the effectiveness of our strategy against complex tuberculosis cases (particularly drug-resistant strains) requires further validation. Addressing these challenges will significantly accelerate the clinical translation of our findings.

5. Conclusions

We developed mannose-modified nebulizable nanoemulsions for the treatment of tuberculosis. These nanoemulsions exhibit excellent inhalation properties, enabling targeted penetration into tuberculous granulomas and demonstrating good co-localization with *M. tuberculosis*. They possess significant antibacterial efficacy *in vivo* along with anti-inflammatory activity. We contend that the programmed diversity within pulmonary macrophages is currently underappreciated in existing drug and vaccine development pipelines. The strategic harnessing of macrophage heterogeneity through targeted remodeling holds significant potential to boost the efficacy of novel anti-tuberculosis therapies. Our rationally designed co-delivery platform coordinates temporal-spatial control of two therapeutic actions: apoptosis-initiated immunomodulation that dismantles the protective granuloma architecture, and antibiotic-triggered bactericidal activity against now-vulnerable mycobacteria. This ‘niche disruption−pathogen clearance’ strategy marks a fundamental shift in therapeutic design, effectively overcoming the physiological barriers that have long limited conventional tuberculosis treatment. More broadly, this targeted approach establishes a novel treatment paradigm and may offer a new conceptual framework and experimental basis for the treatment of other refractory pulmonary infections.

Acknowledgements

This work was supported by grants from the National Natural Science Foundation of China (82404528 and 82341083), the Noncommunicable Chronic Diseases-National Science and Technology Major Project (2023ZD0506105/2023ZD0506100 to Weimin Li, China), the China Postdoctoral Science Foundation under Grant Number 2024M762259, the Sichuan Science and Technology Program (2024NSFSC1735 and 2026NSFSCZY0142, China), the Postdoctoral Fellowship Program (Grade B) of China Postdoctoral Science Foundation (GZB20240506, China), the Postdoctoral Program of West China Hospital, Sichuan University (2024HXBH018, China), the 1.3.5 Project of State Key Laboratory of Respiratory Health and Multimorbidity (RHM24208,

China), the 1.3.5 Project of Disciplines Excellence (ZYYC23027, China), the State Key Laboratory Special Fund (2060204, China), the Chinese Academy of Medical Sciences Innovation Fund for Medical Sciences (2023-12M-2-001, China).

Author contributions

Weimin Li, Xun Sun, Hairui Wang, and Chengdi Wang: conceptualization, supervision, funding acquisition. Hairui Wang, Jinghong Xian, Guonian Zhu, Zhiqiang Xie, Yongshun Zhang, Lan Yang, Yunming Zhang, Teng Li and Yehui Zhou: investigation, formal analysis. Hairui Wang, Jinghong Xian, Chengdi Wang: resources. Hairui Wang, Guonian Zhu, Chengdi Wang, Xun Sun: methodology. Hairui Wang, Xun Sun, and Chengdi Wang wrote the original draft; Weimin Li, Xun Sun, Hairui Wang, Guangsheng Du, and Chengdi Wang supervised the study and acquired funding. All authors have approved the final manuscript.

Conflicts of interest

The authors declare no competing interests.

Appendix A. Supporting information

Supporting information to this article can be found online at https://doi.org/10.1016/j.apsb.2026.02.026.

References

1. Trajman A, Campbell JR, Kunor T, Ruslami R, Amanullah F, Behr MA, et al. Tuberculosis. *Lancet* 2025;**405**:850−66.
2. World Health Organization. Global tuberculosis report 2024. Available from: https://www.who.int/teams/global-tuberculosis-programme/tb-reports/global-tuberculosis-report-2024.
3. Gai X, Allwood B, Sun Y. Advances in the awareness of tuberculosis-associated chronic obstructive pulmonary disease. *Chin Med J Pulm Crit Care Med* 2024;**2**:250−6.
4. Dartois VA, Rubin EJ. Anti-tuberculosis treatment strategies and drug development: challenges and priorities. *Nat Rev Microbiol* 2022;**20**:685−701.
5. Lenaerts A, Barry 3rd CE, Dartois V. Heterogeneity in tuberculosis pathology, microenvironments and therapeutic responses. *Immunol Rev* 2015;**264**:288−307.
6. Davis JM, Ramakrishnan L. The role of the granuloma in expansion and dissemination of early tuberculous infection. *Cell* 2009;**136**:37−49.
7. Prideaux B, Via LE, Zimmerman MD, Eum S, Sarathy J, O'Brien P, et al. The association between sterilizing activity and drug distribution into tuberculosis lesions. *Nat Med* 2015;**21**:1223−7.
8. Dean AS, Tosas Auguet O, Glaziou P, Zignol M, Ismail N, Kasaeva T, et al. 25 years of surveillance of drug-resistant tuberculosis: achievements, challenges, and way forward. *Lancet Infect Dis* 2022;**22**:e191−6.
9. Farhat M, Cox H, Ghanem M, Denkinger CM, Rodrigues C, Abd El Aziz MS, et al. Drug-resistant tuberculosis: a persistent global health concern. *Nat Rev Microbiol* 2024;**22**:617−35.
10. Khan A, Abbas M, Verma S, Verma S, Rizvi AA, Haider F, et al. Genetic variants and drug efficacy in tuberculosis: a step toward personalized therapy. *Glob Med Genet* 2022;**9**:90−6.
11. van Ingen J, Hoefsloot W, Dartois V, Dick T. Rifampicin has no role in treatment of mycobacterium avium complex pulmonary disease and bactericidal sterilising drugs are needed: a viewpoint. *Eur Respir J* 2024;**63**:2302210.
12. Chandra P, Grigsby SJ, Philips JA. Immune evasion and provocation by mycobacterium tuberculosis. *Nat Rev Microbiol* 2022;**20**:750−66.
13. Zhai W, Wu F, Zhang Y, Fu Y, Liu Z. The immune escape mechanisms of mycobacterium tuberculosis. *Int J Mol Sci* 2019;**20**:340.
14. Russell DG, Simwela NV, Mattila JT, Flynn J, Mwandumba HC, Pisu D. How macrophage heterogeneity affects tuberculosis disease and therapy. *Nat Rev Immunol* 2025;**25**:370−84.
15. Gong Z, Han S, Liang T, Zhang H, Sun Q, Pan H, et al. Mycobacterium tuberculosis effector PPE36 attenuates host cytokine storm damage *via* inhibiting macrophage M1 polarization. *J Cell Physiol* 2021;**236**:7405−20.
16. Sha S, Shi Y, Tang Y, Jia L, Han X, Liu Y, et al. Mycobacterium tuberculosis Rv1987 protein induces M2 polarization of macrophages through activating the PI3K/Akt1/mTOR signaling pathway. *Immunol Cell Biol* 2021;**99**:570−85.
17. Russell DG, Simwela NV, Mattila JT, Flynn J, Mwandumba HC, Pisu D. How macrophage heterogeneity affects tuberculosis disease and therapy. *Nat Rev Immunol* 2025;**25**:370−84.
18. Singh M, Sarhan MO, Damiba NNL, Singh AK, Villabona-Rueda A, Nino-Meza OJ, et al. Proapoptotic Bcl-2 inhibitor as potential host directed therapy for pulmonary tuberculosis. *Nat Commun* 2025;**16**:3003.
19. Stutz MD, Allison CC, Ojaimi S, Preston SP, Doerflinger M, Arandjelovic P, et al. Macrophage and neutrophil death programs differentially confer resistance to tuberculosis. *Immunity* 2021;**54**:1758−71.e7.
20. Mei Q, Luo P, Zuo Y, Li J, Zou Q, Li Y, et al. Formulation and *in vitro* characterization of rifampicin-loaded porous poly (epsilon-caprolactone) microspheres for sustained skeletal delivery. *Drug Des Devel Ther* 2018;**12**:1533−44.
21. Nair A, Greeny A, Nandan A, Sah RK, Jose A, Dyawanapelly S, et al. Advanced drug delivery and therapeutic strategies for tuberculosis treatment. *J Nanobiotechnology* 2023;**21**:414.
22. Fenaroli F, Repnik U, Xu Y, Johann K, Van Herck S, Dey P, et al. Enhanced permeability and retention-like extravasation of nanoparticles from the vasculature into tuberculosis granulomas in zebrafish and mouse models. *ACS Nano* 2018;**12**:8646−61.
23. Li B, Wang W, Zhao L, Wu Y, Li X, Yan D, et al. Photothermal therapy of tuberculosis using targeting pre-activated macrophage membrane-coated nanoparticles. *Nat Nanotechnol* 2024;**19**:834−45.
24. Zhang C, D'Angelo D, Buttini F, Yang M. Long-acting inhaled medicines: present and future. *Adv Drug Deliv Rev* 2024;**204**:115146.
25. Zhou QT, Leung SS, Tang P, Parumasivam T, Loh ZH, Chan HK. Inhaled formulations and pulmonary drug delivery systems for respiratory infections. *Adv Drug Deliv Rev* 2015;**85**:83−99.
26. Lin J, Yang L, Liu T, Zhao H, Liu Y, Shu F, et al. Mannose-modified exosomes loaded with MiR-23b-3p target alveolar macrophages to alleviate acute lung injury in Sepsis. *J Control Release* 2025;**379**:832−47.
27. Tian JH, Huang S, Wang ZH, Li JJ, Song X, Jiang ZT, et al. Supramolecular discrimination and diagnosis-guided treatment of intracellular bacteria. *Nat Commun* 2025;**16**:1016.
28. Wilson RJ, Li Y, Yang GZ, Zhao CX. Nanoemulsions for drug delivery. *Particuology* 2022;**64**:85−97.
29. Guo Y, Bera H, Shi C, Zhang L, Cun D, Yang M. Pharmaceutical strategies to extend pulmonary exposure of inhaled medicines. *Acta Pharm Sin B* 2021;**11**:2565−84.
30. Shirley M. Amikacin liposome inhalation suspension: a review in mycobacterium avium complex lung disease. *Drugs* 2019;**79**:555−62.
31. Liu Q, Zhang X, Xue J, Chai J, Qin L, Guan J, et al. Exploring the intrinsic micro-/nanoparticle size on their *in vivo* fate after lung delivery. *J Control Release* 2022;**347**:435−48.
32. Wang H, Luo S, Xie M, Chen Z, Zhang Y, Xie Z, et al. ACE2 receptor-targeted inhaled nanoemulsions inhibit SARS-CoV-2 and attenuate inflammatory responses. *Adv Mater* 2024;**36**:e2311537.
33. Seow HC, Cai JP, Pan HW, Luo C, Wen K, Situ J, et al. Neutralisation of SARS-CoV-2 by monoclonal antibody through dual targeting powder formulation. *J Control Release* 2023;**358**:128−41.
34. Li X, Wang Q, Huang J, Yue X, Zhang X, Fan X, et al. Posaconazole nanocrystals dry powder inhalers for the local treatment of invasive pulmonary aspergillosis. *Int J Pharm* 2025;**668**:124938.

35. He J, Lin X, Zhang D, Hu H, Chen X, Xu F, et al. Wake biofilm up to enhance suicidal uptake of gallium for chronic lung infection treatment. *Biomaterials* 2024;**310**:122619.
36. Miao Y, Zhang H, Wang C, Li P, Chen L, Kang Z, et al. Inhalable nanovaccine based on bioengineered bacteria-derived membrane vesicles against lung metastasis. *Adv Mater* 2026;**38**:e06174.
37. Tian Y, Ding B, Ma ZR, Yang JT, Ding GT, Liu HN. Study on physicochemical properties, fatty acids, texture, antioxidant and antibacterial activities of ghee from different regions. *J Dairy Sci* 2023;**106**:7419−31.
38. Kim YG, Lee JH, Lee J. Antibiofilm activities of fatty acids including myristoleic acid against cutibacterium acnes *via* reduced cell hydrophobicity. *Phytomedicine* 2021;**91**:153710.
39. Sidders AE, Kedziora KM, Arts M, Daniel JM, de Benedetti S, Beam JE, et al. Antibiotic-induced accumulation of lipid II synergizes with antimicrobial fatty acids to eradicate bacterial populations. *eLife* 2023;**12**:e80246.
40. Shariq M, Quadir N, Alam A, Zarin S, Sheikh JA, Sharma N, et al. The exploitation of host autophagy and ubiquitin machinery by mycobacterium tuberculosis in shaping immune responses and host defense during infection. *Autophagy* 2023;**19**:3−23.
41. Warner DF, Mizrahi V. The survival kit of mycobacterium tuberculosis. *Nat Med* 2007;**13**:282−4.
42. Bekale RB, Maphasa RE, D'Souza S, Hsu NJ, Walters A, Okugbeni N, et al. Immunomodulatory nanoparticles induce autophagy in macrophages and reduce mycobacterium tuberculosis burden in the lungs of mice. *ACS Infect Dis* 2025;**11**:610−25.
43. Bekale RB, Du Plessis SM, Hsu NJ, Sharma JR, Sampson SL, Jacobs M, et al. Mycobacterium tuberculosis and interactions with the host immune system: opportunities for nanoparticle based immunotherapeutics and vaccines. *Pharm Res* 2018;**36**:8.
44. Blomgran R, Desvignes L, Briken V, Ernst JD. Mycobacterium tuberculosis inhibits neutrophil apoptosis, leading to delayed activation of naive CD4 T cells. *Cell Host Microbe* 2012;**11**:81−90.
45. Divangahi M, Desjardins D, Nunes-Alves C, Remold HG, Behar SM. Eicosanoid pathways regulate adaptive immunity to mycobacterium tuberculosis. *Nat Immunol* 2010;**11**:751−8.
46. Kumar NP, Moideen K, Banurekha VV, Nair D, Babu S. Plasma proinflammatory cytokines are markers of disease severity and bacterial burden in pulmonary tuberculosis. *Open Forum Infect Dis* 2019;**6**:ofz257.
47. Vivekanandan MM, Adankwah E, Aniagyei W, Acheampong I, Yeboah A, Arthur JF, et al. Plasma cytokine levels characterize disease pathogenesis and treatment response in tuberculosis patients. *Infection* 2023;**51**:169−79.
48. Gupte AN, Kumar P, Araujo-Pereira M, Kulkarni V, Paradkar M, Pradhan N, et al. Baseline IL-6 is a biomarker for unfavourable tuberculosis treatment outcomes: a multisite discovery and validation study. *Eur Respir J* 2022;**59**:2100905.